RESEARCH ARTICLE

Key Points:
- Bedform migration adds another mode of pore water transport
- Bedform migration strongly attenuates benthic fluxes
- Dispersion has a strong effect in case of bedform migration

Supporting Information:
- Movie S1
- Supporting Information S1

Correspondence to:
S. Ahmerkamp,
sahmerka@mpi-bremen.de

The impact of bedform migration on benthic oxygen fluxes

Soeren Ahmerkamp[1], Christian Winter[2], Felix Janssen[1,3,4], Marcel M. M. Kuypers[1], and Moritz Holtappels [1,2]

[1]Max Planck Institute for Marine Microbiology, Bremen, Germany, [2]MARUM Center for Marine Environmental Sciences, Bremen, Germany, [3]Helmholtz Centre for Polar and Marine Research, Bremerhaven, Germany, [4]HGF-MPG Group for Deep Sea Ecology and Technology, Bremen, Germany

Abstract Permeable sediments are found wide spread in river beds and on continental shelves. The transport of these sediments is forced by bottom water currents and leads to the formation of bedforms such as ripples and dunes. The bottom water flow across the bedforms results in pressure gradients that drive pore water flow within the permeable sediment and enhance the supply of reactive substrates for biogeochemical processes. This transport-reaction system has been extensively studied for the case of stationary bedforms, whereas bedform migration—the most ubiquitous form of sediment transport—has been often ignored. To study the impact of sediment transport on pore water flow, we incorporated an empirical model of bedform migration into a numerical transport-reaction model for porous media, using oxygen as reactive solute. The modeled oxygen flux changes significantly as soon as the sediment divides into an upper mobile layer (migrating bedform) and a stationary layer underneath. The bedform is increasingly flushed with oxic bottom water, whereas pressure gradients and pore water flow reverse at increasing rate underneath the bedform. This suppresses net pore water displacement and reduces the oxygen penetration depth up to 90%. In effect, the overall oxygen uptake decreases significantly with bedform migration although bottom water velocities increase. This counterintuitive effect is systematically described for a range of different sediment types, current velocities, and respiration rates and should be considered in future studies.

1. Introduction

Although the coastal ocean comprises less than 20% of the entire ocean area, it sustains more than 50% of the global marine production [*Wollast*, 1991] and is thus a hot spot for nutrient and organic matter cycling. In coastal areas, shallow water depths and enhanced mixing of the water column result in a tight coupling between pelagic primary production and benthic degradation of organic matter and thus a fast recycling of nutrients. Exposed to surface gravity waves, such as tides and wind-generated waves, coastal sediments undergo frequent redistribution and sorting, leaving behind coarser grained (sandy) sediments, which cover approximately 50–70% of coastal areas [*Huettel et al.*, 2014; *Emery*, 1968]. The presence of various bedforms, such as dunes and ripples, is indicative of sediment transport and a continuously changing seabed topography [*Kösters and Winter*, 2014]. The interaction of bottom water flow and bedform topography in combination with the high permeability of sandy sediments leads to a pressure-driven advective pore water flow [*Thibodeaux and Boyle*, 1987] which is most widespread in coastal waters [*Santos et al.*, 2012; *Huettel et al.*, 1996] and rivers [*Thibodeaux and Boyle*, 1987; *Rutherford et al.*, 1993, 1995]. Solute fluxes between the sediment pore space and overlying water may be several orders of magnitude higher compared to diffusion-dominated systems [*Huettel et al.*, 2014]. Pore water advection enhances solute exchange but also the influx of particulate organic matter which is retained in the sediment and fuels microbial activity [*Huettel and Rusch*, 2000]. Comprehensive in situ studies have shown that advective pore water flow can cause a tenfold increase of net oxygen uptake in intertidal sediments [*de Beer et al.*, 2005; *Precht et al.*, 2004]. Also, high-denitrification rates in these sediments have been reported [*Marchant et al.*, 2014; *Gao et al.*, 2012; *Rao et al.*, 2008; *Gao et al.*, 2010] which may counteract the increased riverine and atmospheric nitrogen input to coastal areas, emphasizing the ecological importance of these sediments.

Using either numerical and analytical models [*Cardenas et al.*, 2008; *Grant et al.*, 2014], flume studies [*Precht and Huettel*, 2003], or in situ studies [*Reimers et al.*, 2004], the effects of advective pore water flow in permeable sediments have been studied almost exclusively for the case of stationary, i.e., nonmigrating bedforms.

Although bedforms are known to undergo constant changes, only very few flume experiments have considered the effect of sediment transport and bedform evolution on benthic microbial processes [*Precht et al.*, 2004], and no systematic studies have been performed so far. Bedform migration needs to be considered to fully address pore water transport but adds another level of complexity and another boundary condition in mass transport modeling. In many model studies boundary conditions are handled independently from each other [*Bardini et al.*, 2012; *Kessler et al.*, 2013, 2015] even though well established empirical models exist that link for example bedform migration to bottom water velocity or sediment grain diameter to permeability [*Coleman and Melville*, 1994; *Gangi*, 1985]. Applying these relations reduces the number of possible parameter combinations and allows investigating the integrated response of the pore water flow to changing boundary conditions. To our knowledge, there are no systematic quantifications of net fluxes that cover a wide range of natural conditions.

In this model study the dynamic transport of solutes and sediments as found under realistic conditions is simulated by introducing bedform migration to the transport-reaction equation. By non-dimensionalizing transport-reaction equations, the range of parameter values is extended to cover a large variety of possible in situ conditions. Empirical models are applied to relate bedform migration and permeability to the median grain size of the sediment, so that the magnitude of the resulting net fluxes are finally controlled by grain size, bottom water velocity, and microbial activity (in terms of volumetric respiration rates), i.e., by parameters that may easily be measured and quantified under field conditions.

2. Methods

A multiphysical approach is used that couples a turbulence-resolving, large eddy simulation (LES)-type hydrodynamical model of the bottom water flow with the pore water flow in the porous Darcy domain. The LES domain and the Darcy domain are separated by a single bedform (see Figure 1). Based on the bedform height η, the dimensions in the water column are in longitudinal direction 10η and in transversal as well as vertical direction 5η. The Darcy domain is two dimensional and extents 15η in vertical direction and 10η in longitudinal direction. Similar to previous studies [*Cardenas and Wilson*, 2007], a sequential approach couples the water column—the upper domain—with the benthic domain below. The pressure distribution along the bedform surface is extracted from the LES model and used as boundary condition for benthic pore water advection which is solved following Darcy's law. The bedform migration is considered in the transport-reaction equation by using a frame of reference that moves at the speed and in direction of the migrating bedform, for which a simple coordinate transformation is sufficient (Figure 3b). This approach simplifies the calculations and is physically identical to the use of a moving grid. The migration celerity is determined by an empirical model based on sediment grain size and the bed shear stress, which is directly extracted from the LES model. Another empirical model is used to relate grain size to permeability.

The model equations are used in non-dimensional formulation, and their derivation is presented in the supporting information Text S2. In the following, most variables are shown as non-dimensional variables. Dimensional variables are marked by bold characters.

2.1. Model Formulation

Large eddy simulations are used to resolve the turbulent flow above the bedform, the larger energy-containing coherent structures are resolved, and the smaller scales at which energy dissipates are parameterized. Mathematically, this is performed by the spatial filtering of the Navier-Stokes and continuity equation [see also *Scalo et al.*, 2012a]:

$$\frac{\partial \bar{u}_i}{\partial x_i} = 0 \tag{1}$$

$$\frac{\partial \bar{u}_i}{\partial t} + \frac{\partial \bar{u}_i \bar{u}_j}{\partial x_j} = -\frac{\partial \bar{p}}{\partial x_i} + \frac{1}{Re}\frac{\partial^2 \bar{u}_i}{\partial x_j \partial x_j} - \frac{\partial \tau_{ij}}{\partial x_j} - \frac{\mathbf{f}}{\rho \mathbf{U}^2}\delta_{1j} \tag{2}$$

Here δ_{ij} is the Kronecker delta, $Re = \mathbf{U}\boldsymbol{\eta}/\nu$ is the Reynolds number, where $\mathbf{U}$ is the bottom water velocity (average velocity at the upper boundary), $\boldsymbol{\eta}$ is the bedform height, and ν is the kinematic viscosity of sea water. The spatial coordinates are represented by x_i where x_1 is the longitudinal direction, x_2 is the wall-normal direction, and x_3 is the transversal direction. $\bar{u}_i$ is the filtered velocity vector, and t is the time. The overbar denotes spatially averaged quantities. Further, ρ is the density, p is the pressure, and $\mathbf{f}$ is the forcing term
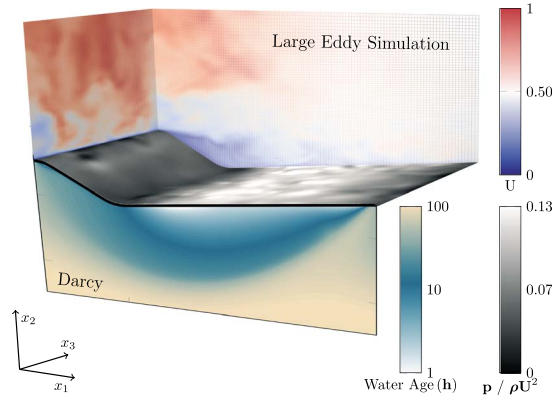
Figure 1. Instantaneous bottom water velocity (red to blue) and pressure distribution (black to white) along the bedform for $Re = 2400$. The LES domain is coupled to the Darcy domain via the averaged pressure distribution. The pseudocolors in the Darcy domain indicate the water age.

which is a constant longitudinal pressure gradient. $\tau_{ij} = \overline{u_j u_j} - \bar{u}_i \bar{u}_j$ are the subgrid stresses, not resolved by the grid. This subgrid scale is modeled by means of a dynamic model using the Lagrangian averaging technique [*Charles Meneveau and Cabot*, 1996]. The Navier-Stokes equations are solved in the OpenFoam® environment based on the pisoFoam solver. The following equations are implemented into the source code (see also Text S1).

The bottom water flow field causes a pressure gradient at the sediment-water interface which drives pore water advection in the porous domain. The model solves Darcy's law in the porous domain and the continuity equation [*Cardenas and Wilson*, 2007; *Scalo et al.*, 2012a]:

$$u_{p,i} = -Re\frac{k}{\phi}\frac{\partial <p>}{\partial x_i} \tag{3}$$

$$\frac{\partial u_{p,i}}{\partial x_i} = 0 \tag{4}$$

where k is the permeability and ϕ is the porosity and $u_{p,i}$ is the pressure-driven pore water velocity. The chevron brackets $<>$ denote temporal averages of the dynamic pressure at the sediment-water interface. Averaged over a period of 1 min, the pressure distribution was found to be stable. The sediment acts as a low-pass filter for the mass transport, and therefore, temporal fluctuations are neglected.

Above a critical bottom water velocity, the bed shear stress at the sediment-water interface will cause mobilization of sediment and thus sediment transport. For a given rippled seabed, sediment is continuously eroded at the stoss side of the ripples and deposited at the lee side which causes a train-like bedform migration (Figure 3b). Associated with sediment erosion and deposition is the release of pore water at the stoss side and trapping of bottom water at the lee side, respectively. The exchange of pore and bottom water during bedform migration is implemented into the transport-reaction equation below by means of a coordinate transformation (see supporting information Text S3). The result is an additional advection term in longitudinal direction. The non-dimensional transport-reaction equation reads

$$\phi\frac{\partial C}{\partial t} + \phi\frac{\partial}{\partial x_i}\left[(u_{p,i} - c_{ph}\delta_{1j})\,C\right] = \phi\frac{\partial}{\partial x_i}\left[\left(\frac{1}{Pe} + D_t\right)\frac{\partial C}{\partial x_i}\right] - R_c \tag{5}$$

where C is the solute concentration, c_{ph} the bedform celerity after the coordinate transformation, and $Pe = \mathbf{U}\boldsymbol{\eta}/\mathbf{D}$ is the Péclet number, where $\mathbf{D}$ denotes the molecular diffusion. The dispersion coefficient D_t is implemented after *Bear and Buchlin* [1978] in tensorial formulation. D_t is a function of $u_{p,i}$ multiplied with factors for the longitudinal (α_L) and transversal dispersion (α_T). α_T and α_L control the smearing of solute concentration gradients in porous media, i.e., the diffusion like displacement of water parcels along the flow path. The longitudinal component α_L is in the range of the sediment pore size, while the transversal component is at least 1 order of magnitude smaller [*Bear and Buchlin*, 1978]. The reaction term R_c depends on the concentration and follows the Monod kinetic:

$$R_c = Dak\frac{C}{K_m + C} \tag{6}$$

where $Dak = R \cdot Re$ is the Damköhler Number (described below), R is the maximum reaction rate, and K_m is the half-saturation coefficient. The transport-reaction equation and Darcy equation are non-dimensionalized following *Scalo et al.* [2012b] and *Higashino et al.* [2004] (see supporting information Text S2). The parameter values used in this study are shown in Table 1. As stated above, bold symbols denote dimensional quantities, whereas normal style symbols denote dimensionless quantities.

Table 1. Model Parameters and Sources

		Scaled by	Natural Range	Values Adopted	Reference
$\boldsymbol{\eta}$ (m)	Bedform Height		0.005 m – 0.1 m	0.02 m	*Janssen et al.* [2012]
H (m)	Half Channel Height		0.4		*Janssen et al.* [2012]
ν (m^2/s)	Kinematic Viscosity		$1.1 \cdot 10^{-6}$ m^2 s^{-1}	$1.1 \cdot 10^{-6}$ m^2/s	*Weast et al.* [1988]
λ (m)	Bedform Length	η	-	0.2 m	*Janssen et al.* [2012]
ϕ	Porosity		0.3 – 0.6	0.4	*Huettel et al.* [2014]
U (m s^{-1})	Bottom Water Velocity		0.1 – 1 m/s	0.1 – 0.9 m/s	*Kösters and Winter* [2014]
U$_p$ (m s^{-1})	Pore Water Flow	**U**	$10^{-4} - 10^{-5}$ m/s	$10^{-3} - 10^{-7}$ m/s[b]	*Reimers et al.* [2004]
k (m^2)	Intrinsic Permeability	η^2	$10^{-10} - 10^{-12}$ m^2	$10^{-10} - 10^{-12}$ m^2	*Wilson et al.* [2008]
Δp	Pressure Head	$\rho \mathbf{U}^2$	0.06 – 0.1	0.1	*Huettel et al.* [1996][a]
α (m)	Relative Dispersion	α_L / α_T	8 – 24	10	*Bear and Buchlin* [1978]
α_L	Longitudinal Dispersion	η	$(1.4 - 7.3) \cdot 10^{-3}$ m	$2 \cdot 10^{-3}$ m	*Rao et al.* [2007][b]
c$_{ph}$ (m s^{-1})	Bedform Migration	**U**	0.1 – 90 cm h^{-1}	0 – 200 cm h^{-1}	*Miles and Thorpe* [2015]
C$_0$ (μmol l^{-1})	Oxygen Concentration	**C**	$<350 \mu$mol l^{-1}	280 μmol l^{-1}	*Weast et al.* [1988]
R (μmol l^{-1} h^{-1})	Volumetric Consumption Rate	$\mathbf{C U}^2 / \nu$	(10 – 100) μmol l^{-1} h^{-1}	(10 – 180) μmol l^{-1} h^{-1}	*de Beer et al.* [2005]
K$_m$ (μmol l^{-1})	Half Saturation Constant	**C**	35 μmol l^{-1}	-	
	Dimensionless Numbers	Equation			
Re	Reynolds Number	$\mathbf{U}\eta / \nu$	-	1000 – 15000	
U$_p$	Pore water Flow[c]	$2k \frac{Re}{\phi} \frac{\Delta p}{\lambda}$	-	$10^{-2} - 10^{-6}$	
Pe	Péclet Number	$ReScU_p$	-	0.1 – 300	
Sc	Schmidt Number	ν / D	-	500	

[a]The pressure data by *Huettel et al.* [1996] was non-dimensionalized using $\rho \mathbf{U}^2$.

[b]The dispersion coefficients calculated by *Rao et al.* [2007] where used to estimate α_L ($\alpha_L = \mathbf{D}_t \mathbf{U}_f^{-1}$, where $\mathbf{U}_f$ is the pore water velocity imposed in the core incubations).

[c]The values of U_p are calculated based on the model setup, but the range is shown for comparison.

2.2. Bedform Migration

The mechanistics of bedform initialization, development, and migration are still not fully understood. Thus, migration velocities must be based on empirical relations, which predict either the sediment transport or the bedform migration itself [*Bhaganagar and Hsu*, 2009]. For this investigation the migration is implemented using an empirical description after *Coleman and Melville* [1994], which has been derived from flume experiments:

$$\mathbf{c}_{ph} = \frac{\left(\frac{\eta}{\mathbf{d}_g} - 3.5 \right)^{1.3}}{40} \cdot (\mathbf{u}_\tau - \mathbf{u}_{\tau cr})(\theta - \theta_{cr}) \tag{7}$$

where $\mathbf{d}_g$ is a characteristic grain diameter, $\mathbf{u}_\tau = (\tau / \rho)^{0.5}$ and $\mathbf{u}_{\tau cr} = (\tau_{cr} / \rho)^{0.5}$ are the shear velocity and critical shear velocity, respectively, where τ is the bed shear stress and ρ the water density. Further, the bed shear stress is non-dimensionalized and represented as the Shields parameter $\theta = \tau / [(\rho_s - \rho)\mathbf{g d}_g]$ and critical Shields parameter $\theta_{cr} = \tau_{cr} / [(\rho_s - \rho)\mathbf{g d}_g]$. The critical shields parameter defines the threshold for the initialization of motion. Here we use an empirical relation based on the non-dimensional grain size, i.e., Bonneville parameter, after *Soulsby* [1997].

Coleman and Melville [1994] determined the shear velocity by fitting the logarithmic law of the wall [*Karman*, 1930] to the velocity profile for flat bed conditions. *Coleman and Melville* [1994] based the Reynolds number on the half channel height (H) $Re_c = \mathbf{U}H / \nu$. Using $\mathbf{u}_\tau$, the friction Reynolds number can be defined as $Re_\tau = \mathbf{u}_\tau \eta / \nu$. The experimental data of *Coleman and Melville* [1994] suggests that Re_τ increases linearly with Re_c on a logarithmic scale and can be approximated by

$$Re_\tau \approx 0.02 Re_c^{1.10} \tag{8}$$

The fit is shown in Figure 2a. This relationship has the advantage that it can be directly integrated into the equations.
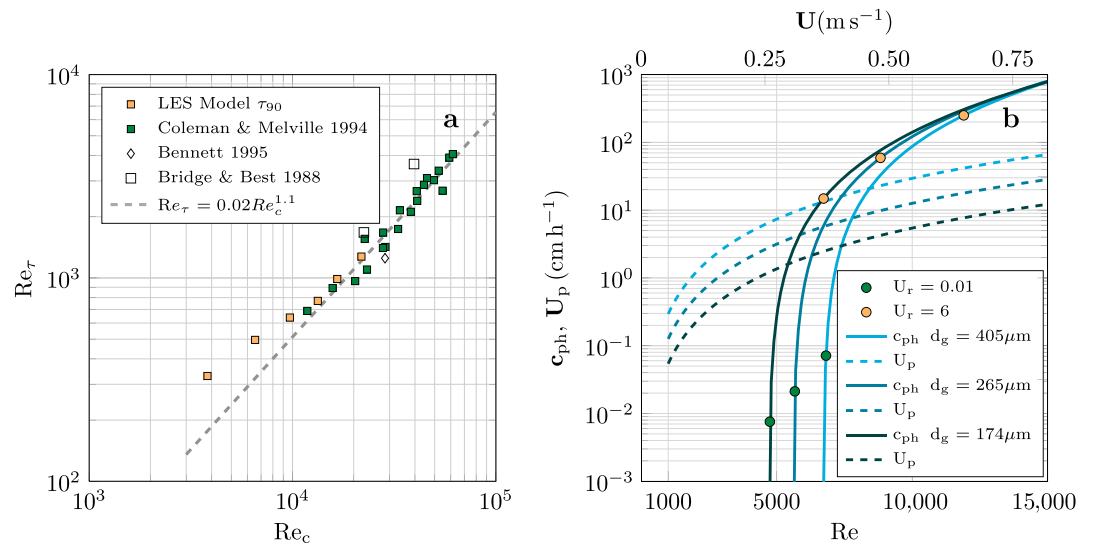
Figure 2. (a) Linear scaling of the friction Reynolds number Re_τ with channel Reynolds Re_c number including data from various authors. The linear fit is based on data by *Coleman and Melville* [1994]. (b) Bedform celerity (c_{ph}) and pressure-driven advective pore water flow (U_p) for different characteristic grain sizes as a function of the Reynolds number. The quantities are scaled for a representative bedform height of $\eta = 0.02$ m.

2.3. Governing Non-dimensional Numbers

The characteristics of the modeled system are described by non-dimensional numbers, representing the relative dominance of different forces, time scales, or transport processes. Besides the Reynolds number, we introduce the velocity ratio U_r which relates the pressure-induced pore water velocity and the bedform celerity c_{ph}:

$$U_r = \frac{c_{ph}}{U_p} \tag{9}$$

U_p is the characteristic pore water velocity induced by the pressure gradient (derived from Darcy's law) and defined as

$$U_p = 2\,\mathbf{k}\frac{\mathbf{U}}{\phi \mathbf{v}}\frac{\Delta p}{\lambda} = 2\frac{kRe}{\phi}\frac{\Delta p}{\lambda} \tag{10}$$

where λ is the ripple length and Δp the non-dimensional characteristic pressure difference, which is the pressure induced by the hydraulic head. From a pressure distribution Δp can be calculated as the difference between pressure maximum and pressure minimum or 2 times the amplitude of the main harmonic signal. Therefore, U_p can be seen as the maximum pore water velocity induced by the characteristic pressure along half the bedform length $\lambda/2$. The flow field induced by the pressure gradient is two dimensional, with varying pore water velocities along different pathlines. A concise description is difficult, and therefore, the definition of a characteristic pore water flow is useful.

Using U_p, the Péclet number for the porous media can be determined as

$$Pe_p = \frac{\eta \mathbf{U}}{\mathbf{D}}U_p = Pe\,U_p \tag{11}$$

which defines the ratio of advective to diffusive timescales.

Due to the two dimensional velocity field, fast and slow pathlines co-occur in the sediment with highest velocities generally found in the vicinity of the sediment surface. The competition between the transport rate and the reaction rate, here oxygen respiration, is expressed by the first-order Damköhler number (henceforth Damköhler number):

$$Dak_p = \frac{\mathbf{R}}{\mathbf{C}_0}\frac{\eta}{\mathbf{U}U_p} = \frac{ReR}{U_p} \tag{12}$$

where C_0 is the concentration of oxygen in the bottom water. The Damköhler number compares the relative rates of advective transport to reaction. If $Dak_p > 1$, the oxygen respiration dominates and controls the distribution and fate of oxygen. Most of the oxygen is consumed close to the sediment-water interface. If $Dak_p < 1$, the system is transport dominated and oxygen penetrates deep into the bedform and is partially recirculated back to the overlying water.

2.4. Model Setup and Parametrization

All parameter values used in this study are shown in Table 1. The bedform geometry of *Janssen et al.* [2012] (bedform height and length: $\eta = 0.02$ m and $\lambda = 0.2$ m) was adopted as a reference for this investigation. *Janssen et al.* [2012] performed experiments in a flume with permeable bedforms that were exposed to unidirectional flow in 0.1 m water depth to study advective pore water flow and its forcing by the current velocity. The bedform geometry controls the pore water flow and thus the residence time of a solute in the sediment [*Rutherford et al.*, 1993] and therefore determines—in combination with reaction rates—the solute flux between pore water and bottom water. It is known that the bedform wavelength scales with the grain size: 1000 $\mathbf{d}_g$ with an aspect ratio η/λ of approximately 7–10 [*Soulsby*, 1997; *Van Rijn et al.*, 1993; *Yalin*, 1972], which encompasses the here presented geometry. Testing different bedform geometries exceeds the scope of this investigation.

Preceding publications focusing on biogeochemical processes inside the sediment have often neglected dispersion effects. However, the transversal dispersion does strongly enhance the retention time of solutes in pore water [*Elliott and Brooks*, 1997a; *Bottacin-Busolin and Marion*, 2010]. The longitudinal dispersion adopted in the present work is based on measurements for continental shelf sediments [$\alpha_L = 2 \cdot 10^{-3}$ m *Rao et al.*, 2007], whereas the transversal dispersion is calculated based on experimental data where a ratio of α_T/α_L between 8 and 24 was found [*Bear and Buchlin*, 1978].

This study focusses on oxygen fluxes, with oxygen being the energetically most favorable electron acceptor which often governs the distribution of other electron acceptors such as nitrate, iron and manganese oxides. Three typical pore water reaction rates are tested: low respiration (10 µmol l^{-1} h^{-1}), medium respiration (90 µmol l^{-1} h^{-1}), and high respiration (180 µmol l^{-1} h^{-1}). The grain size distribution determines the permeability and the bedform celerity (see above). On continental shelves characteristic grain diameters of permeable sediments typically vary between $\mathbf{d}_g = 150$ µm and $\mathbf{d}_g = 500$ µm [*Kösters and Winter*, 2014]. Here grain sizes of 174 µm, 265 µm, 405 µm were considered. Different empirical relations exist linking permeabilities to grain sizes. Here we used $\mathbf{k} = Da \cdot 735 \cdot 10^6 \cdot d_g^2$ (where Da is the conversion factor for unit Darcy into m^2 (= $9.869 \cdot 10^{-13}$)), which resulted in permeabilities of $2.2 \cdot 10^{-11}$ m^2, $5.1 \cdot 10^{-11}$ m^2, and $1.5 \cdot 10^{-10}$ m^2 [*Gangi*, 1985].

The following different model experiments were carried out: The LES-derived pressure distribution along the bedform surface and the wall shear were extracted for six different Reynolds numbers ($Re = 1500$–$10,000$, with corresponding bottom water velocities of $\mathbf{U} = 5$–80 cm s^{-1}). As a validation of the LES model, the pressure distribution along the bedform was compared to measurements of *Janssen et al.* [2012] ($\mathbf{U} = 12$ cm s^{-1}, $Re = 2200$). Then the transport-reaction equation for the porous domain was solved, including oxygen respiration and bedform migration. The Reynolds number, i.e., the bottom water velocity, was increased subsequently from $Re = 1000$–$15,000$ in intervals of 250. This procedure was repeated for three different grain sizes, three respiration rates, and two dispersion factors (with/ without dispersion) which sums up to a total of approximately 1000 model experiments.

3. Results

3.1. Model Validation

The pressure distribution on the bedform surface drives the advective pore water flow inside permeable sediments. In Figure 3a the pressure distribution derived from the LES model is presented. Along the upstream slope of the ripple the time-averaged (1 min interval) pressure increases to a maximum in the middle of the stoss side. The global minimum is found close to the crest, whereas at the lee side a low pressure plateau is found.

The pressure distribution is in strong agreement with the measurements of *Janssen et al.* [2012] suggesting that the LES model is capable to reproduce realistic conditions. Compared to the modeled pressure distribution obtained using a Reynolds-averaged Navier-Stokes (RANS) approach [*Janssen et al.*, 2012], deviations to
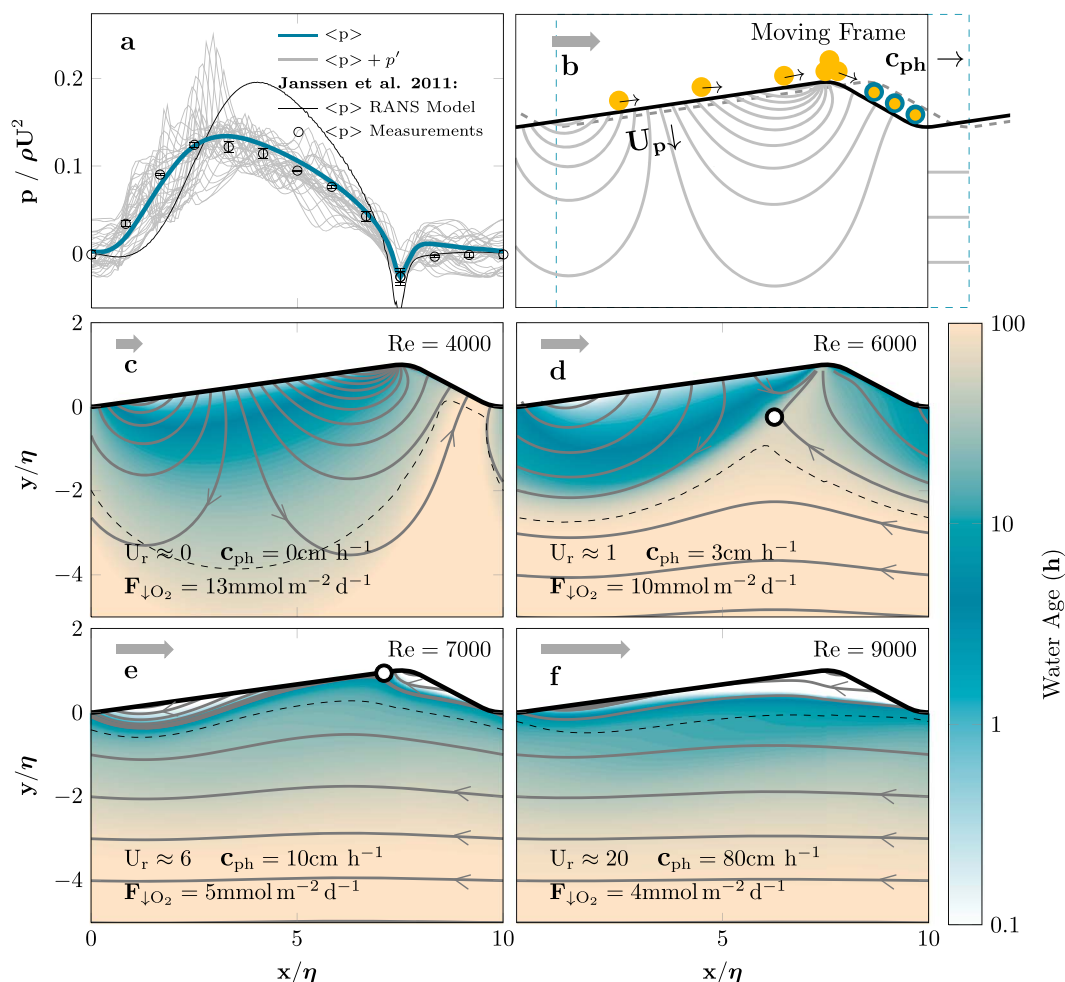
Figure 3. (a) LES-derived pressure distribution along the bedform surface in comparison to measurements and a preceding RANS approach. (b) Schematics of the moving frame are shown. The yellow bullets represent sediment grains, which get mobilized when the critical Shields parameter is exceeded. At the lee side of the bedform the blue contours around the grains illustrate the trapping of pore water accompanied with grain deposition. (c–f) Effect of bedform migration for increasing Reynolds numbers. The corresponding grain size is $d_g = 174$ µm, and the bedform height is scaled by $\eta = 0.02$ m. Therefore, the Reynolds numbers correspond to bottom water velocities of $U = 22, 33, 39$, and 50 cm s^{-1} as indicated by the grey arrows. The color denotes the age of water after entering the sediment. The dashed line indicates the oxygen penetration depth for a reaction rate of $R = 10$ µmol l^{-1} h^{-1}. The black circle indicates the point of stagnation, where the advective pore water flow and bedform migration are the same in magnitude and direction. Solid grey lines indicate the streamlines.

the measured pressure distribution were considerably smaller for the LES. This becomes especially visible for the local pressure in the region at the stoss side where the flow reattaches. Here the LES model shows strong fluctuations of the instantaneous pressure distribution due to the turbulent structures that encounter the bedform stoss side. The averaged pressure distribution itself is also similar to dunes where η is of $\mathcal{O}(10$ cm) [*Fehlman*, 1985].

By extracting the pressure from the LES model, a characteristic pressure difference (spacial pressure head variation) can be estimated as $\Delta p \approx 0.1$ (2 times the amplitude of the pressure distribution in Figure 3a which can be approximated as $\Delta p = 2\sqrt{2}\sigma$ where σ is the standard deviation of the pressure). For Reynolds numbers varying between $Re = 2000$ and $Re = 10,000$ only minimal deviations are found between the non-dimensional pressure distributions, as well as the characteristic difference Δp. Therefore, the distribution presented can be scaled by ρU^2. This is in agreement with prior investigations [*Cardenas and Wilson*, 2007], which found that the location of eddy reattachment and the pressure distribution barely change for varying flow conditions. In previous laboratory experiments with bedform heights ranging from 1 cm ripples to 20 cm dunes the

characteristic pressure head was found to vary between $\Delta p = 0.06$ and $\Delta p = 0.1$ [*Huettel et al.*, 1996; *Fehlman*, 1985; *Elliott and Brooks*, 1997a] (recalculated values).

To estimate the bedform celerity, the bed shear stress can directly be calculated from the LES model. Insertion of the spacial averaged bed shear stress in equation (7) would underestimate the shear stress that is actually responsible for the sediment erosion at the stoss side, because the average value is lowered by the values in the trough [*Bhaganagar and Hsu*, 2009]. Therefore, τ_{90} the 90th percentile of the bed shear stress is extracted and used as the governing shear stress, which is in good agreement with measurements [*Coleman and Melville*, 1994; *Bennett and Best*, 1995; *Bridge and Best*, 1988] as shown in Figure 2a. The increase of the friction Reynolds number with the channel Reynolds number is well presented by equation (8). Henceforth, equation (8) is used for varying Reynolds numbers to determine the bed shear and subsequently the migration celerity. In Figure 2b typical migration celerities are shown for the considered grain sizes. In continental shelve regions migration celerities were measured and found to vary in similar ranges $\mathbf{c}_{ph} = 0.1 – 4$ cm h^{-1} [*Traykovski et al.*, 1999] and in intertidal systems up to $\mathbf{c}_{ph} = 90$ cm h^{-1} [*Miles and Thorpe*, 2015].

3.2. Solute Transport for Migrating Bedforms

With the resolved pressure distribution at the sediment surface, the advective pore water flow inside the sediment is calculated and inserted into the transport-reaction equation (5). To simulate the range of natural environmental conditions, the transport-reaction equations were solved stationary ($\frac{\partial C}{\partial t} = 0$, i.e., no changes over time) for different bottom water velocities, grain sizes, and oxygen respiration rates, which includes a corresponding range of permeabilites and bedform migration velocities derived from the empirical relations. As an example, the patterns of solute transport are shown for a grain size of $\mathbf{d}_g = 174$ μm, a reaction rate of $\mathbf{R} = 10$ μmol l^{-1} h^{-1} and for four different current velocities, i.e., four different Reynolds numbers (Figures 3c–3f and Movie S1).

The bedform migration is directly coupled to the shear velocity; therefore, the bottom water flow determines if and how fast the bedform migrates. In Figure 3c the water age (age of a water parcel following the streamlines) under a bedform is shown for $Re = 4000$, $\mathbf{U} = 0.22$ m s^{-1}, where no migration is predicted. The distribution of the pore water age and the oxygen penetration depth (i.e., the isoline where 99% of oxygen is consumed) is in agreement with patterns observed [*Ziebis et al.*, 1996; *Elliott and Brooks*, 1997b] and modeled before [*Cardenas et al.*, 2008]. The solute penetrates from the stoss side into the bedform and is consumed along the pathline. The water age distribution indicates that old pore water is released at the lee side of the bedform along a chimney-like structure. The penetration depth reaches down to 6 cm (based on $\boldsymbol{\eta} = 0.02$ m), which is distinctly deeper than for pure diffusion [*Glud*, 2008]. The streamlines start and end at the sediment surface.

At the onset of bedform migration (Figure 3d), the porous matrix of the sediment divides into an upper mobile layer and a stationary layer underneath. The deposition of sand grains at the lee side of the bedform traps bottom water, while sediment erosion at the stoss side causes the release of pore water. Thus, an exchange of bottom and pore water takes place due to the moving porous matrix. However, it does not cause a flow within the porous matrix. True pore water flow is driven only by pressure gradients from current-bedform interactions. Nevertheless, bedform migration is highly effective because it leads to oscillating pressure gradients and flow reversals in the sediment layers below the bedform. At certain depths, pressure gradients reverse too fast and pore water flow is too slow to allow for a substantial net vertical displacement. At these depths solute transport is driven only by dispersion and diffusion. Although dispersion increases with pore water velocity, it cannot compensate the hindered advective transport. As a result, the two interfering transport processes of bedform migration and pressure-driven pore water flow cause the separation of a flushed upper layer from a sealed lower layer.

In Figure 3d, the layer separation is visualized by the different orientation of the streamlines, which reflect the sum of the pressure-driven pore water flow and the longitudinal movement of the reference frame. Streamlines that start and end at the sediment surface denote the layer where pressure-driven pore water flow from surface to surface takes less time than it takes the bedform to migrate over a full bedform length. Thus, an exchange with bottom water still takes place. In contrast, the horizontal streamlines at depth denote the layer where pore water flow reverses before reaching the sediment surface. The streamlines start and end in the sediment, and their vertical deflection shows the amplitude of the vertical pore water oscillation.

Another emerging feature is the point of stagnation (circle in Figures 3d–3e) which occurs where the velocities of pressure-driven pore water flow and bedform migration are equal in magnitude and direction
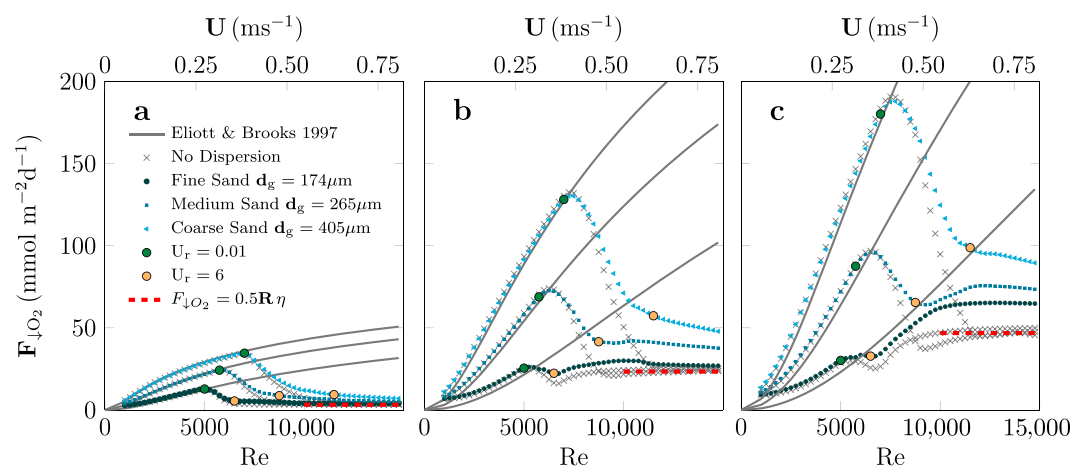
Figure 4. Net fluxes for different reaction rates (a) $\mathbf{R} = 10$ µmol l^{-1} h^{-1}, (b) $\mathbf{R} = 90$ µmol l^{-1} h^{-1}, and (c) $\mathbf{R} = 180$ µmol l^{-1} h^{-1} and grain sizes $\mathbf{d}_g = 174, 265,$ and $405,$ µm along increasing Reynolds numbers. The second abscissa shows the bottom water velocity for a corresponding bedform height of $\boldsymbol{\eta} = 0.02$ m. The red line indicates the oxygen net flux for a fully flushed bedform.

[*Bottacin-Busolin and Marion*, 2010]. It is the upper most point of the sealed layer and moves upward as bedform migration is further increased (see Movie S1). At the arrival of the point of stagnation at the sediment-water interface (see also Figure 3e), bedform migration starts dominating over the characteristic pore water flow ($U_r = 6$) (Figure 3e). Here the shape of the oxygen distribution changes distinctly. Most of the oxygen enters the bedform at the lower stoss side where pressure is highest and close to the crest at the lee side due to bedform migration and pore water trapping. The oxygen penetration depth is strongly reduced, but the flushed regions have high pore water velocities which lead to very low pore water ages.

When bedform migration is further increased ($U_r > 6$) (Figure 3f), the bedform celerity fully dominates over the pressure-driven pore water flow, and hence, no point of stagnation is found anymore. The solute penetration from the stoss side is mostly hindered, and the bedform is fully flushed due to the combined sediment deposition and pore water trapping at the lee side. In summary, with increasing bedform migration, gradients of pore water age and oxygen change from a two-dimensional to a one-dimensional vertical orientation, i.e., anoxic pore water, is always found underneath oxic pore water but not in the same layer. Because the pressure distribution is tied to the fast migrating bedform, frequent vertical reversal of the pore water flow suppresses any net vertical advective transport underneath the bedforms. However, pore water is still moving upward and downward, and this movement in combination with dispersion and diffusion controls the solute transport at greater depth.

3.3. Impact of Bedform Migration on Net Oxygen Fluxes

The net flux of oxygen across the sediment-water interface is estimated for three exemplary grain sizes, three oxygen respiration rates, and for bottom water velocities ranging from $\mathbf{U} = 5-80$ cm s^{-1} ($Re = 1000-15,000$, $\boldsymbol{\eta} = 0.02$ m) both with and without dispersion. These parameters cover typical ranges for North Sea sediments as summarized in Table 1. Evolutions of the associated net oxygen fluxes with increasing Reynolds number are summarized in Figure 4.

The net oxygen fluxes for different grain sizes and oxygen respiration rates vary in magnitude but react in similar ways to increasing bottom water velocities. For stationary bedforms (no migration) the net oxygen fluxes strongly increase with bottom water velocity. As soon as the shear stress and Shields parameter exceed their critical value, the bedform starts to migrate ($U_r > 0$). For increasing bottom water velocities the net oxygen fluxes are affected by the increasing migration celerity and start to drop off at $U_r > 0.01$ ($\mathbf{c}_{ph} = 0.01, 0.1,$ and 0.5 cm h^{-1}). The ascending U_r indicates that the migration celerity increases faster than the advective pore water flow (compare Figure 2b).
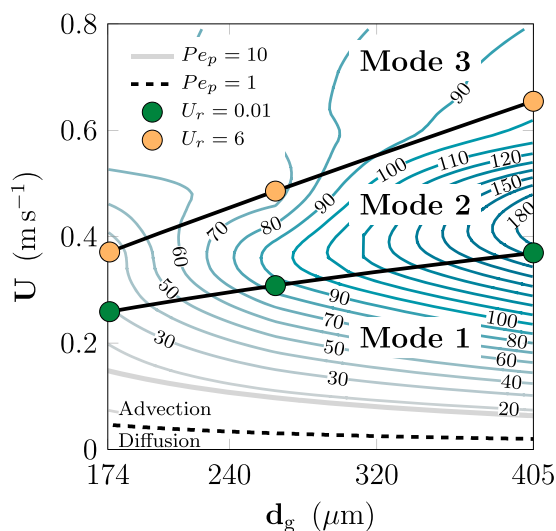
Figure 5. Governing modes of pore water flow shown in the phase space of grain size and bottom water velocity. Isolines indicate oxygen net fluxes (in mmol m^{-2} d^{-1}) for a reaction rate of $\mathbf{R} = 180$ µmol l^{-1} h^{-1}. The migration celerities for $\mathbf{U}_r = 0.01$ are $\mathbf{c}_{ph} = 0.01, 0.1,$ and 0.5 cm h^{-1} and $\mathbf{c}_{ph} = 10, 55,$ and 200 cm h^{-1} for $\mathbf{U}_r = 6$.

The net oxygen fluxes decrease further until the ratio of migration celerity to characteristic pore water flow is well above unity ($U_r \approx 6$). In Figure 4 this equilibrium is visible as a local minimum (see also Figure 3e). The point of stagnation arrives at the sediment-water interface. A further increase of the bottom water velocity leads to domination of bedform migration ($U_r > 6$, $\mathbf{c}_{ph} = 10, 55,$ and 200 cm h^{-1}). The net fluxes approach a saturation plateau, which is defined by the theoretical net flux calculated for a fully flushed bedform. At the plateau the role of dispersion for the solute supply to deeper sediment layers becomes clearly visible. Without dispersion, the fluxes converge fast toward the theoretical net flux. For cases with dispersion the net fluxes do not converge. They slowly drop off and remain clearly above the theoretical net flux. This behavior becomes more pronounced for higher respiration rates ($\mathbf{R} = 90$ µmol l^{-1} h^{-1} and $\mathbf{R} = 180$ µmol l^{-1} h^{-1}).

With increasing respiration rates, the oxygen fluxes increase strongly. For the smallest respiration rate $\mathbf{R} = 10$ µmol l^{-1} h^{-1} (Figure 4a) the fluxes vary in between 1 and 50 mmol m^{-2} d^{-1}. The transport rates are dominating the respiration rates as reflected in an average Damköhler number (average for all bottom water velocities) smaller than unity. The penetrating front reaches deep into the bedform, and a substantial amount of oxic pore water is released without being consumed. For higher respiration rates $\mathbf{R} = 90$ µmol l^{-1} h^{-1} and $\mathbf{R} = 180$ µmol l^{-1} h^{-1} (Figures 4b and 4c) the respiration rates dominate over transport rates yielding average Damköhler numbers larger than unity. Most of the oxygen that enters the bedform is consumed close to the surface leading to increased net fluxes between 20 and 190 mmol m^{-2} d^{-1}.

Considering that the bed shear stress, responsible for the bedform migration, is a function of the bottom water velocity, the net flux is controlled by three parameters, namely, grain size, bottom water velocity, and respiration rate. This relationship is summarized in the phase space of grain size and bottom water velocity (Figure 5) for a respiration rate $\mathbf{R} = 180$ µmol l^{-1} h^{-1}. Larger grain sizes shift the onset of bedform migration towards higher bottom water velocities. In combination with the enhanced permeability the fluxes are strongly increased. For example, for the largest grain size $\mathbf{d}_g = 405$µm the twofold increased permeability, compared to $\mathbf{d}_g = 265$µm, leads to a net flux difference of approximately 50 mmol m^{-2} d^{-1} for $U = 0.25$ m s^{-1}. On the other hand, the increase of the $U_r = 0.01$ line—bedform migration occurs at higher bottom water velocities for larger grain sizes—leads to a total difference of 90 mmol m^{-2} d^{-1} between the two maxima for $\mathbf{d}_g = 405$ µm and $\mathbf{d}_g = 275$ µm, emphasizing the importance of the grain size.

4. Discussion and Environmental Implications

This study investigates the effect of bedform migration on benthic exchange fluxes using an interlinked and thus realistic forcing of pressure-driven pore water flow and bedform migration.

Similar to many previous studies [e.g., *Kessler et al.*, 2013; *Cardenas and Wilson*, 2007; *Kessler et al.*, 2015] and for the sake of computational efficiency the model was based on a few simplifying assumptions. We neglected microscale transport processes at the very sediment surface such as shear-driven flow in the Brinkman layer [*Brinkman*, 1949] and turbulent pressure fluctuations [*Scalo et al.*, 2012b; *Higashino et al.*, 2004]. These processes affect the upper 100 µm to mm of the sediment [*Goharzadeh et al.*, 2005; *Kaviany*, 2012] which is negligible compared to the shift of penetration depths of a few centimeters found in this study (see Figure 3). Further, bedform migration is implemented by using a moving frame of reference, which assumes a stable bedform geometry that does not change over the range of applied bottom water velocities (U = 5–80 cm s^{-1}).

This is a valid assumption for unidirectional flow in the absence of waves [e.g., *Baas*, 1994; *Richards*, 1980] and was also used in previous model studies [*Bottacin-Busolin and Marion*, 2010; *Elliott and Brooks*, 1997a; *Kessler et al.*, 2015]. The maximum applied bottom water velocity (80 cm s^{-1}) was within the range of velocities (up to 90 cm s^{-1}) used by *Coleman and Melville* [1994] to establish the empirical relation for bedform migration. However, bottom water velocities beyond the upper range (75–80 cm s^{-1}), as found in, e.g., fast flowing rivers, can cause a change in bedform geometry and a subsequent wash out of the bedform [*Raudkivi*, 1997], which is not reflected by the model. At such velocities much of the upper sediment layer is mobilized and gets hypersaturated. This layer would behave like a fluid with strongly altered permeabilities. For the here applied conditions the bedforms are quasi-static with respect to the bottom water velocity and the extent of the mobile sheet layer is negligible. Fast flowing rivers with high bed permeability may exhibit a significant underflow velocity of the pore water induced by stream gradients [e.g., *Bottacin-Busolin and Marion*, 2010]. However, this is not considered here because stream gradients are not present in continental shelf sediments. Even for river sediments in the permeability range used in this study and typical stream gradients of order centimeter per kilometer, the underflow velocity is an order of magnitude smaller than the smallest characteristic pore water flow in this study and can thus be neglected.

The model results indicate that bedform migration should not be ignored and may strongly attenuate flux estimates based on models assuming stationary bedforms or plain beds. The empirical coupling of the governing transport parameters, i.e., the dependence of permeability and migration celerity on grain size and bottom water velocity, allows for the distinction of three different modi of pore water transport in permeable sediments (Figure 5):

Mode 1. The bedform is stationary, and pressure-driven advective pore water flow is dominant ($U_r \ll 1$), resulting in a deep solute penetration and high oxygen uptake rates.

Mode 2. The competition of bedform migration and advective-driven pore water flow leads to the formation of a redox seal. The deeper sediment layer shows suppressed vertical net transport which decreases with increasing bottom water velocities ($U_r = 0.01$–6).

Mode 3. Bedform migration is dominant, and only the bedform itself is well flushed ($U_r > 6$). The transport in the sediment below is controlled by diffusion and dispersion and fluxes stagnate at low values, independent of further acceleration of the bottom water velocity.

The general patterns of solute distributions (Figure 3) were previously observed in flume experiments [*Precht et al.*, 2004] for a narrow range of boundary conditions. The here presented model is capable of simulating oxygen fluxes based on a few parameters, i.e., grain size, bottom water velocity, and respiration rate, as summarized in Figure 5.

In a semianalytical approach *Elliott and Brooks* [1997a] investigated the residence time of a conservative solute in the sediment for the simplified case of a constant sinusoidal pressure head over a flat bed. By introducing solute reactivity and after reformulation of the model (see equations S.21–S.28 in the supporting information of Text S4), we found that the fluxes for stationary bedforms are determined by the bedform length and Damköhler number, which can be estimated from experiments and in situ measurements. Despite the simplifying assumptions of the traditional Elliot model, it compares well with our model (10% maximum deviation) for the case of stationary bedforms (Figure 4). However, at migrating bedforms, the pressure-driven advective pore water flow is deteriorated by bedform migration and our model strongly deviates from the Elliot model, because the latter do not consider bedform migration. Fast bedform migration and the resulting fast vertical flow reversal lead to a suppression of net pore water displacement and the formation of a redox seal [*Huettel et al.*, 2014] which separates deeper anoxic regions from the oxic bedform above. The strength of the concentration gradient and the oxygen flux between these two layers depends on the dispersive transport. While no dispersion and no diffusion would lead to a step change of oxygen concentrations, the up and down movement of water parcels in combination with dispersion enhances the gradient-driven downward transport [*Bottacin-Busolin and Marion*, 2010]. The effect can be significant as shown for the case of high oxygen respiration rates in fine sand, i.e., high Damköhler numbers, where increasing bedform migration even enhances the oxygen fluxes at moderate and high reaction rates (Figure 4). This setting may be found on intertidal flats where respiration rates in fine sand are in the range of 100 μmol l^{-1} h^{-1} and larger [*de Beer et al.*, 2005; *Gao et al.*, 2012].

In contrast to our finding, negligible effect of bedform migration on oxygen uptake and denitrification was reported in a recent model study that simulated migrating bedforms using a travelling sinusoidal pressure

distribution over a flat bed [*Kessler et al.*, 2015]. The travelling speed (i.e., bedform migration) was coupled neither to bottom water velocity nor to sediment grain size, and results were presented only for a single reaction rate (100 µmol l^{-1} h^{-1}) and a single permeability (4·10^{-11} m^2). However, such a reduced parameter combination cannot thoroughly capture the effect of bedform migration but reflects a rather specific solution. Even in our study there are specific parameter combinations that, taken separately, could lead to biased conclusions. In Figure 4b, for example, the effect of bedform migration seems negligible for a reaction rate of 90 µmol l^{-1} h^{-1} and a grain size of 174 µm (permeability of 2.2·10^{-11} m^2) — parameter values that are comparable to those used by [*Kessler et al.*, 2015] — whereas for the majority of parameter combinations the effect is clearly visible. The high dispersion coefficient is another possible reason why the effect of bedform migration was not observed in *Kessler et al.* [2015]. The dispersivity controls the vertical solute transport across the established redox seal. Especially for a flat bed model in which bedform elevation is neglected, dispersion is the only way to exchange solutes between sediment and water column when bedform migration is fast. The effect of bedform migration can be strongly reduced by an increased dispersivity, and indeed, a dispersion coefficient of 1 cm used in *Kessler et al.* [2015] is rather high of $\mathcal{O}(\eta)$ and not of pore scale magnitude.

The modeled oxygen fluxes as a function of bottom water velocity, grain size, and reaction rates vary widely between 3 and 190 mmol m^{-2} d^{-1} which is comparable to the range of measured oxygen uptake rates. Eddy correlation measurements, which may provide the most realistic oxygen uptake rates for permeable sediments [*Berg et al.*, 2003], revealed that oxygen uptake of marine subtidal sands can vary between 3 and 30 mmol m^{-2} d^{-1} [*Reimers et al.*, 2012; *Berg et al.*, 2013; *McGinnis et al.*, 2014], whereas for intertidal systems, where nutrient availability and organic matter input is high, net oxygen fluxes were found to range between $\mathbf{F}_{\downarrow O_2}$ = 105 mmol m^{-2} d^{-1} and $\mathbf{F}_{\downarrow O_2}$ = 170 mmol m^{-2} d^{-1} [*de Beer et al.*, 2005].

In this study, the complex pore water transport was investigated as the main controlling variable for benthic oxygen uptake. However, the oxygen sink within the sediment, i.e., the distribution of the maximum oxygen reaction rate (R), was assumed to be similar throughout the porous domain. The maximum reaction rate usually depends on the availability of labile particulate organic matter. Different from solutes, particles can be retained in the pore space and its accumulation depends largely on the filtration capacity of the sands [*Rusch et al.*, 2001]. In contrast, bedform migration and the accompanied sediment erosion may remove particulate organic matter and thus may counteract the accumulation by filtration. It is likely that reaction rates are regulated by the transport dynamics of particulate organic matter and may show considerable differences with sediment depth. Further, the here presented oxygen uptake is simplified since it does not consider the oxidation of reduced substrates that diffuse upward from deeper sediment layers. However, the implementation of empirical or mechanistic models to parameterize the reaction rate, and abiotic oxidation is a task for future studies.

In conclusion, the integrated model approach allows for investigating complex transport processes that control sediment biogeochemistry and benthic exchange rates. The results strongly suggest that sediment transport such as bedform migration has a significant impact on pore water transport, solute distributions, and benthic net fluxes. This has to be considered in order to understand the dynamic processes in sandy sediments and especially their function as natural filter systems in coastal waters.

References

Baas, J. H. (1994), A flume study on the development and equilibrium morphology of current ripples in very fine sand, *Sedimentology*, *41*(2), 185–209, doi:10.1111/j.13653091.1994.tb01400.x.

Bardini, L., F. Boano, M. Cardenas, R. Revelli, and L. Ridolfi (2012), Nutrient cycling in bedform induced hyporheic zones, *Geochim. Cosmochim. Acta*, *84*, 47–61, doi:10.1016/j.gca.2012.01.025.

Bear, J., and J.-M. Buchlin (1978), *Modelling and Applications of Transport Phenomena in Porous Media*, vol. 5, Kluwer Acad., Dordrecht, Netherlands.

Bennett, S., and J. Best (1995), Mean flow and turbulence structure over fixed, two-dimensional dunes: Implications for sediment transport and bedform stability, *Sedimentology*, *42*(3), 491–513, doi:10.1111/j.1365-3091.1995.tb00386.x.

Berg, P., H. Röy, F. Janssen, V. Meyer, B. B. Jörgensen, M. Huettel, and D. De Beer (2003), Oxygen uptake by aquatic sediments measured with a novel non-invasive eddy-correlation technique, *Mar. Ecol. Prog. Ser.*, *261*(1), 75–83, doi:10.3354/meps261075.

Berg, P., M. H. Long, M. Huettel, J. E. Rheuban, K. J. McGlathery, R. W. Howarth, K. H. Foreman, A. E. Giblin, and R. Marino (2013), Eddy correlation measurements of oxygen fluxes in permeable sediments exposed to varying current flow and light, *Limnol. Oceanogr.*, *58*(4), 1329–1343, doi:10.4319/lo.2013.58.4.1329.

Bhaganagar, K., and T.-J. Hsu (2009), Direct numerical simulations of flow over two-dimensional and three-dimensional ripples and implication to sediment transport: Steady flow, *Coast. Eng.*, *56*(3), 320–331, doi:10.1016/j.coastaleng.2008.09.010.

Bottacin-Busolin, A., and A. Marion (2010), Combined role of advective pumping and mechanical dispersion on time scales of bedform-induced hyporheic exchange, *Water Resour. Res.*, *46*, W08518, doi:10.1029/2009WR008892.

Bridge, J. S., and J. L. Best (1988), Flow, sediment transport and bedform dynamics over the transition from dunes to upper-stage plane beds: Implications for the formation of planar laminae, *Sedimentology*, *35*(5), 753–763, doi:10.1111/j.1365-3091.1988.tb01249.x.

Brinkman, H. (1949), A calculation of the viscous force exerted by a flowing fluid on a dense swarm of particles, *Appl. Sci. Res.*, *1*(1), 27–34, doi:10.1007/BF02120313.

Cardenas, M. B., and J. L. Wilson (2007), Dunes, turbulent eddies, and interfacial exchange with permeable sediments, *Water Resour. Res.*, *43*, W08412, doi:10.1029/2006WR005787.

Cardenas, M. B., P. L. Cook, H. Jiang, and P. Traykovski (2008), Constraining denitrification in permeable wave-influenced marine sediment using linked hydrodynamic and biogeochemical modeling, *Earth Planet. Sci. Lett.*, *275*(1), 127–137, doi:10.1016/j.epsl.2008.08.016.

Charles Meneveau, T. S. L., and W. H. Cabot (1996), A Lagrangian dynamic subgrid-scale model of turbulence, *J. Fluid Mech.*, *319*, 353–385, doi:10.1017/S0022112096007379.

Coleman, S. E., and B. W. Melville (1994), Bed-form development, *J. Hydraul. Eng.*, *120*, 544–560, doi:10.1061/(ASCE)0733-9429(1994)120.

de Beer, D., F. Wenzhöfer, T. G. Ferdelman, S. E. Boehme, M. Huettel, J. E. van Beusekom, M. E. Böttcher, N. Musat, and N. Dubilier (2005), Transport and mineralization rates in North Sea sandy intertidal sediments, Sylt-Rømø Basin, Wadden Sea, *Limnol. Oceanogr.*, *50*(1), 113–127, doi:10.4319/lo.2005.50.1.0113.

Elliott, A. H., and N. H. Brooks (1997a), Transfer of nonsorbing solutes to a streambed with bedforms: Theory, *Water Resour. Res.*, *33*(1), 123–136, doi:10.1029/96WR02784.

Elliott, A. H., and N. H. Brooks (1997b), Transfer of nonsorbing solutes to a streambed with bedforms: Laboratory experiments, *Water Resour. Res.*, *33*(1), 137–151, doi:10.1029/96WR02783.

Emery, K. (1968), Relict sediments on continental shelves of world, *Am. Assoc. Petroleum Geol. Bull.*, *52*(3), 445–464.

Fehlman, H. M. (1985), Resistance components and velocity distributions of open channel flows over bedforms, PhD thesis, Colorado State Univ., Ft. Collins.

Gangi, A. F. (1985), Permeability of unconsolidated sands and porous rocks, *J. Geophys. Res.*, *90*(B4), 3099–3104, doi:10.1029/JB090iB04p03099.

Gao, H., F. Schreiber, G. Collins, M. M. Jensen, J. E. Kostka, G. Lavik, D. de Beer, H.-y. Zhou, and M. M. Kuypers (2010), Aerobic denitrification in permeable Wadden Sea sediments, *Int. Soc. Microbial Ecol. J.*, *4*(3), 417–426, doi:10.1038/ismej.2009.127.

Gao, H., M. Matyka, B. Liu, A. Khalili, J. E. Kostka, G. Collins, S. Jansen, M. Holtappels, M. M. Jensen, and T. H. Badewien (2012), Intensive and extensive nitrogen loss from intertidal permeable sediments of the Wadden Sea, *Limnol. Oceanogr.*, *57*(1), 185–198, doi:10.4319/lo.2012.57.1.0185.

Glud, R. N. (2008), Oxygen dynamics of marine sediments, *Mar. Biol. Res.*, *4*(4), 243–289, doi:10.1080/17451000801888726.

Goharzadeh, A., A. Khalili, and B. B. Jörgensen (2005), Transition layer thickness at a fluid-porous interface, *Phys. Fluids*, *17*(5), 57102, doi:10.1063/1.1894796.

Grant, S. B., K. Stolzenbach, M. Azizian, M. J. Stewardson, F. Boano, and L. Bardini (2014), First-order contaminant removal in the hyporheic zone of streams: Physical insights from a simple analytical model, *Environ. Sci. Technol.*, *48*(19), 11,369–11,378, doi:10.1021/es501694k.

Higashino, M., C. J. Gantzer, and H. G. Stefan (2004), Unsteady Diffusional mass transfer at the sediment/water interface: Theory and significance for SOD measurement, *Water Res.*, *38*(1), 1–12, doi:10.1016/j.watres.2003.08.030.

Huettel, A., W. Ziebis, and S. Forster (1996), Flow-induced uptake of particulate matter in permeable sediments, *Limnol. Oceanogr.*, *41*, 309–322, doi:10.4319/lo.1996.41.2.0309.

Huettel, M., and A. Rusch (2000), Transport and degradation of phytoplankton in permeable sediment, *Limnol. Oceanogr.*, *45*(3), 534–549, doi:10.4319/lo.2000.45.3.0534.

Huettel, M., P. Berg, and J. E. Kostka (2014), Benthic exchange and biogeochemical cycling in permeable sediments, *Mar. Sci.*, 23–51, doi:10.1146/annurev-marine-051413-012706.

Janssen, F., M. B. Cardenas, A. H. Sawyer, T. Dammrich, J. Krietsch, and D. de Beer (2012), A comparative experimental and multi-physics computational fluid dynamics study of coupled surface-subsurface flow in bedforms, *Water Resour. Res.*, *48*, W08514, doi:10.1029/2012WR011982.

Karman, T. (1930), Mechanische ähnlichkeit und turbulenz, in *Proceedings of 3rd International Congress of Theoretical and Applied Mechanics*, pp. 322–346, Butterworths, London.

Kaviany, M. (2012), *Principles of Heat Transfer in Porous Media*, Springer Science and Business Media, New York.

Kessler, A. J., R. N. Glud, M. B. Cardenas, and P. L. M. Cook (2013), Transport zonation limits coupled nitrification-denitrification in permeable sediments, *Environ. Sci. Technol.*, *47*(23), 13,404–13,411, doi:10.1021/es403318x.

Kessler, A. J., M. B. Cardenas, and P. L. Cook (2015), The negligible effect of bed form migration on denitrification in hyporheic zones of permeable sediments, *J. Geophys. Res. Biogeosci.*, *120*, 538–548, doi:10.1002/2014JG002852.

Kösters, F., and C. Winter (2014), Exploring German bight coastal morphodynamics based on modelled bed shear stress, *Geo-Mar. Lett.*, *34*(1), 21–36, doi:10.1007/s00367-013-0346-y.

Marchant, H. K., G. Lavik, M. Holtappels, and M. M. Kuypers (2014), The fate of nitrate in intertidal permeable sediments, *PloS one*, *9*(8), e104517, doi:10.1371/journal.pone.0104517.

McGinnis, D. F., S. Sommer, A. Lorke, R. N. Glud, and P. Linke (2014), Quantifying tidally driven benthic oxygen exchange across permeable sediments: An aquatic eddy correlation study, *J. Geophys. Res. Oceans*, *119*, 6918–6932, doi:10.1002/2014JC010303.

Miles, J., and A. Thorpe (2015), Bedform contributions to cross-shore sediment transport on a dissipative beach, *Coast. Eng.*, *98*, 65–77, doi:10.1016/j.coastaleng.2015.01.007.

Precht, E., and M. Huettel (2003), Advective pore-water exchange driven by surface gravity waves and its ecological implications, *Limnol. Oceanogr.*, *48*(4), 1674–1684, doi:10.4319/lo.2003.48.4.1674.

Precht, E., U. Franke, L. Polerecky, and M. Huettel (2004), Oxygen dynamics in permeable sediments with wave-driven pore water exchange, *Limnol. Oceanogr.*, *49*(3), 693–705, doi:10.4319/lo.2004.49.3.0693.

Rao, A. M., M. J. McCarthy, W. S. Gardner, and R. A. Jahnke (2007), Respiration and denitrification in permeable continental shelf deposits on the South Atlantic Bight: Rates of carbon and nitrogen cycling from sediment column experiments, *Cont. Shelf Res.*, *27*(13), 1801–1819, doi:10.1016/j.csr.2007.03.001.

Rao, A. M., M. J. McCarthy, W. S. Gardner, and R. A. Jahnke (2008), Respiration and denitrification in permeable continental shelf deposits on the South Atlantic Bight: N_2: Ar and isotope pairing measurements in sediment column experiments, *Cont. Shelf Res.*, *28*(4), 602–613, doi:10.1016/j.csr.2007.11.007.

Raudkivi, A. (1997), Ripples on stream bed, *J. Hydraul. Eng.*, *123*(1), 58–64, doi:10.1061/(ASCE)0733-9429(1997)123:1(58).

Reimers, C. E., H. A. Stecher III, G. L. Taghon, C. M. Fuller, M. Huettel, A. Rusch, N. Ryckelynck, and C. Wild (2004), In situ measurements of advective solute transport in permeable shelf sands, *Cont. Shelf Res.*, *24*(2), 183–201, doi:10.1016/j.csr.2003.10.005.

Reimers, C. E., H. Oezkan-Haller, P. Berg, A. Devol, K. McCann-Grosvenor, and R. D. Sanders (2012), Benthic oxygen consumption rates during hypoxic conditions on the oregon continental shelf: Evaluation of the eddy correlation method, *J. Geophys. Res.*, *117*, C02021, doi:10.1029/2011JC007564.

Richards, K. J. (1980), The formation of ripples and dunes on an erodible bed, *J. Fluid Mech.*, *99*(03), 597–618, doi:10.1017/S002211208000078X.

Rusch, A., S. Forster, and M. Huettel (2001), Bacteria, diatoms and detritus in an intertidal sandflat subject to advective transport across the water-sediment interface, *Biogeochemistry*, *55*(1), 1–27, doi:10.1023/A:1010687322291.

Rutherford, J., G. Latimer, and R. Smith (1993), Bedform mobility and benthic oxygen uptake, *Water Res.*, *27*(10), 1545–1558, doi:10.1016/0043-1354(93)90099-4.

Rutherford, J., J. Boyle, A. Elliott, T. Hatherell, and T. Chiu (1995), Modeling benthic oxygen uptake by pumping, *J. Environ. Eng.*, *121*(1), 84–95, doi:10.1061/(ASCE)0733-9372(1995)121:1(84).

Santos, I. R., B. D. Eyre, and M. Huettel (2012), The driving forces of porewater and groundwater flow in permeable coastal sediments: A review, *Estuarine, Coastal Shelf Sci.*, *98*, 1–15, doi:10.1016/j.ecss.2011.10.024.

Scalo, C., U. Piomelli, and L. Boegman (2012a), High-schmidt-number mass transport mechanisms from a turbulent flow to absorbing sediments, *Phys. Fluids*, *24*(8), 85103, doi:10.1063/1.4739064.

Scalo, C., U. Piomelli, and L. Boegman (2012b), Large-eddy simulation of oxygen transfer to organic sediment beds, *J. Geophys. Res.*, *117*, C06005, doi:10.1029/2011JC007289.

Soulsby, R. (1997), *Dynamics of Marine Sands: A Manual for Practical Applications*, Centre for Advanced Engineering, Univ. of Canterbury, London.

Thibodeaux, L. J., and J. D. Boyle (1987), Bedform-generated convective transport in bottom sediment, *Nature*, *325*, 341–343, doi:10.1038/325341a0.

Traykovski, P., A. E. Hay, J. D. Irish, and J. F. Lynch (1999), Geometry, migration, and evolution of wave orbital ripples at LEO-15, *J. Geophys. Res.*, *104*(C1), 1505–1524, doi:10.1029/1998JC900026.

Van Rijn, L. C., L. C. van Rijn, and L. C. van Rijn (1993), *Principles of Sediment Transport in Rivers, Estuaries and Coastal Seas*, vol. 2, Aqua Publ., Amsterdam.

Weast, R. C., M. J. Astle, and W. H. Beyer (1988), *CRC Handbook of Chemistry and Physics*, vol. 69, CRC Press, Boca Raton, Fla.

Wilson, A. M., M. Huettel, and S. Klein (2008), Grain size and depositional environment as predictors of permeability in coastal marine sands, *Estuarine, Coastal Shelf Sci.*, *80*(1), 193–199, doi:10.1016/j.ecss.2008.06.011.

Wollast, R. (1991), The coastal organic carbon cycle: Fluxes, sources and sinks, in *Ocean Margin Processes in Global Change*, pp. 365–381, Wiley, Chichester, U. K.

Yalin, M. (1972), *Mechanics of Sediment Transport*, vol. 1, Pergamon Press, Oxford, U. K.

Ziebis, W., M. Huettel, and S. Forster (1996), Impact of biogenic sediment topography on oxygen fluxes in permeable seabeds, *Mar. Ecol. Prog. Ser.*, *140*, 227–237, doi:10.3354/meps140227.